Exploring the reinforcing mechanism and micromechanical models for the interphase characteristics in melt mixed XLPE-fumed SiO 2 nanocomposites

Jince Thomas, Minu Elizabeth Thomas, Jiji Abraham, Bejoy Francis, Zakiah Ahmad, Bindu Patanair, Allisson Saiter, Maciej Jaroszewski, Didier Rouxel, Nandakumar Kalarikkal, et al.

Exploring the Reinforcing Mechanism and Micromechanical Models for the Interphase Characteristics in Melt Mixed XLPE-Fumed SiO_2 Nanocomposites

Jince Thomas[1,2], Minu Elizabeth Thomas[3], Jiji Abraham[4], Bejoy Francis[1], Zakiah Ahmad[5], Bindu Patanair [6], Allisson Saiter-Fourcin[6], Maciej Jaroszewski[7], Didier Rouxel[8], Nandakumar Kalarikkal[2], Sabu Thomas[2,9]*

1. Research and Post Graduate Department of Chemistry, St. Berchmans College, Changanassery-686101, Kerala, India.
2. International and Inter University Centre for Nanoscience and Nanotechnology, Mahatma Gandhi University, Kottayam - 686560, Kerala, India.
3. School of Chemical Sciences, Mahatma Gandhi University, Kottayam - 686560, Kerala, India.
4. Department of Chemistry, Vimala College (Autonomous) Thrissur-680009, Kerala, India.
5. Faculty of Civil Engineering, Universiti Teknologi Mara, Shah Alam, Selangor, Malaysia.
6. Normandie Univ, UNIROUEN, INSA Rouen, CNRS, GPM, 76000 Rouen, France.
7. Department of Electrical Engineering Fundamentals, Wroclaw University of Science and Technology, Wybrzeze Wyspianskiego 27, 50-370 Wroclaw, Poland.
8. Institut Jean Lamour, UMR CNRS7198, Universit é de Lorraine, 54000 Vandoeuvre-Lès Nancy, France.
9. School of Energy Materials, Mahatma Gandhi University, Kottayam - 686560, Kerala, India.

*Corresponding author: Sabu Thomas, School of Energy Materials, Mahatma Gandhi University, Kerala, India and International and Inter University Centre for Nanoscience and Nanotechnology, Mahatma Gandhi University, Kerala, India.

Abstract

We present an experimental and theoretical exploration of well-dispersed, distinctively stable, fumed SiO_2 crosslinked polyethylene (XLPE) nanocomposites. The mechanical properties of fumed SiO_2 /XLPE nanocomposites were assessed with different concentrations of fumed SiO_2, which had noticed that network morphology was immensely influential for the performance of mechanical properties. A reasonable exploration of micromechanical models of composites indicated that the theories of Nicolais–Narkis, and Pukanszky provided an excellent fit to yield strength data of the composites considering the effect of the interphase between XLPE and SiO_2. Furthermore, it highlights that the experimental data can be superimposed with the static

micromechanical models of Nicolais–Narkis, and Pukanszky. Owing to the proper dispersion of the SiO_2 nanospheres in the XLPE matrix, the filler-polymer interactions are found to be enhanced. Moreover, it resulted in the excellent insulation properties of the nanocomposites, which makes it a better candidate for electrical cable insulating materials. The combined results of structural characterizations by Fourier Transform Infrared Spectroscopy (FTIR), X-Ray Diffraction (XRD), Differential Scanning Calorimeter (DSC), Dynamic Mechanical Analysis (DMA), Atomic Force, and Transmission Electron Microscopy (AFM, TEM) confirmed the role of fumed SiO_2 as a reinforcing mediator in the current system.

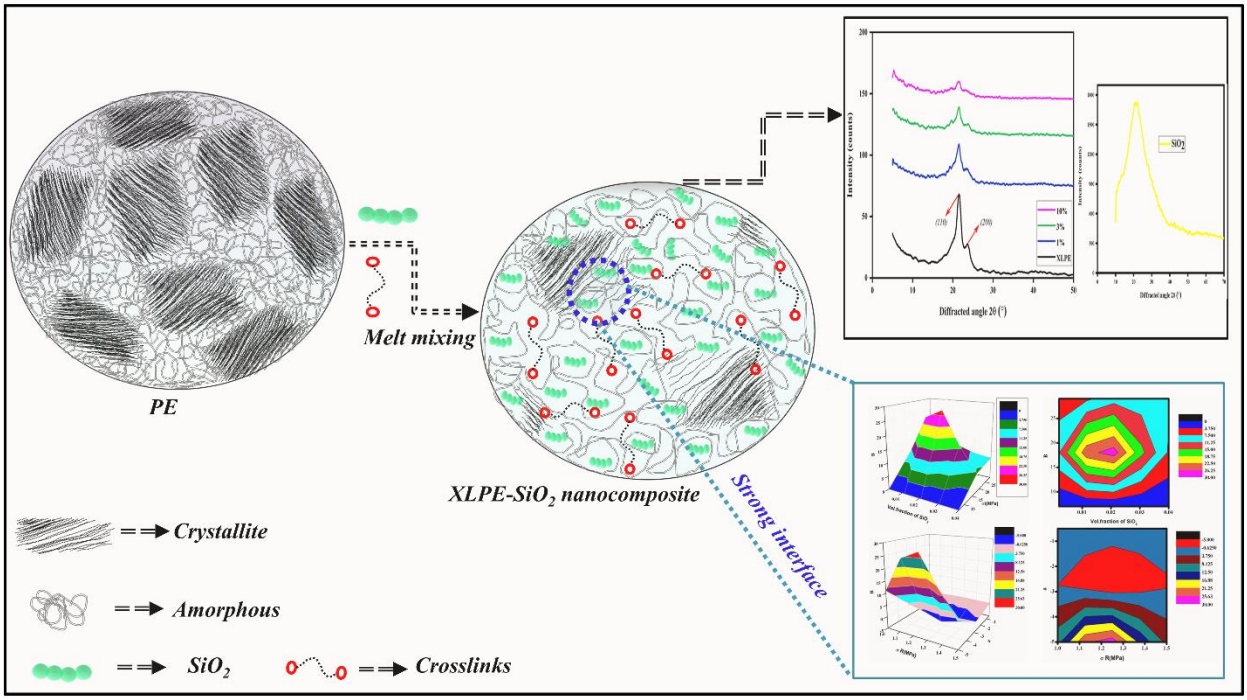

1. Introduction

The primary purpose of insulation is to prevent electrical leakages.[1–3] It helps to maintain the utility of the wire and assure that the conductors are separated electrically and physically within the cable. Therefore, both the safety and effectiveness of the wire or cable depending on the materials are used for insulation. Initially, paper insulation was used in the power industry; however, it was replaced by plastics (thermosets and thermoplastics) later. Crosslinked polyethylene, abbreviated as XLPE, is widely used for insulation purposes because of its high operational temperature, reliability, high dielectric strength, low dielectric loss, chemical resistance, and durability.[4–6] Several studies were reported on XLPE based materials for medium and high voltage cable insulation purposes, and these reports were mainly focused on electrical properties like breakdown strength, partial discharge, electrical treeing, etc.[7–15] To pick the first-class material for the electrical insulation purpose, thorough research on electrical properties and mechanical properties is inevitable.[16–18]

Spherical inorganic SiO_2 nanoparticles can depict innovative and promising nanomaterials due to their unique mechanical, electrical, and thermal insulation properties.[19–21] The outstanding properties of SiO_2 can help make functional and novel engineered polymer nanocomposites for several applications. Fumed SiO_2 based polymer nanocomposites have exceptional mechanical stability, significant electrical and thermal insulation properties at a moderately low concentration of fumed SiO_2. Therefore, fumed SiO_2 based polymer nanocomposites are suitable for cable insulation purposes**.**

In recent years, many research works contributed to understanding the factors that control the morphology-property connection in the polymeric nanocomposites.[22] Parameters such as the type of nanofiller, the volume fraction, the aspect ratio, the dispersion, and the interphase characteristics like strength and modulus will impact the mechanical performances of polymer nanocomposites.[23,24] Also, the large surface area of the nanoparticles aids the formation of a high level of interphase in the nanocomposite, which may provide a powerful interplay between the polymer matrix and the nanofiller (at a low content level).[24] Theoretical studies could help gather more understanding about the interphase and interfacial relations in polymer nanocomposites.[25,26] For the complete interphase property determinations, micromechanical models have been employed in Young's modulus and tensile strength predictions (mechanical properties of polymer

nanocomposites).[27,28] Various techniques have been formulated for modeling purposes in this arena. Pukanszky[29] (1990) developed a semi-empirical formula to predict the effects of filler volume fraction and interfacial interactions on the yield strength of polymer composites. The Pukanszky model is effectively applied for polymer nanocomposites, including nanofillers such as SiO_2, $CaCO_3$, clay, etc.[27,30–32] From the Pukanszky model[29,33], the interaction parameter (B) can be determined from the yield strength of nanocomposites. The parameter 'B' represents the capability of stress transfer between the polymer matrix and particles.

This work divulges how the interfacial parameters influence both static and dynamic mechanical properties of XLPE/ fumed SiO_2 nanocomposites with the help of micromechanical models. This article has proved that filler's reinforcing effect can enhance the mechanical and dielectric properties of polymer systems. XLPE-SiO_2 and SiO_2-SiO_2 interfaces are critical elements in predicting the filler reinforcing effect. The mechanical properties are correlated with the theoretical predictions of Pukanszky's model. The structural characteristics of nanocomposites have been studied by Fourier transform infrared spectroscopy (FTIR), X-Ray Diffraction (XRD), and Differential Scanning Calorimetry (DSC). Atomic Force Microscopy (AFM) and Transmission Electron Microscopy (TEM) data indicated the dispersion of fumed SiO_2 and the interactions of the SiO_2 network in SiO_2 /XLPE nanocomposites.

2. Materials and experimental techniques

Crosslinked polyethylene, density: 0.9-1.0 g/cm^3 provided by Borealis AG (Vienna, Austria) was used for this study. Fumed silica (Cab-O-Sil Ts-720 fumed silica, density: 2.2-2.3 g/cm^3, particle size 40 to 130 nm, obtained from Cabot Corporation, United States) was used as the filler. Dicumyl peroxide (DCP) was used as the cross-linker for forming XLPE. Brabender unit is utilized to mix XLPE and fumed SiO_2 at 150 °C and 60 rpm for 12 minutes. Details for the fabricated nanocomposites are shown in Table 1.

Brabender melt-mixed XLPE nanocomposites were compression molded in an SHP-30 model hydraulic press with a pressure of 100 kg/cm^2 at 180 °C for 5 minutes.[17,34,35]

Table 1: Formulations of XLPE /fumed SiO_2 nanocomposites

Sample name	XLPE (%)	Fumed SiO_2
XLPE	100	0
0.5%	100	0.5%
1%	100	1%
3%	100	3%
5%	100	5%
10%	100	10%

Tensile properties of the nanocomposites were assessed through Universal Testing Machine (Tinius Olsen) at a crosshead speed of 50 mm/min. Dumbbell-shaped samples with sizes of 33 mm in length, 6 mm in width, and 2 mm in thickness were used for the tensile analysis according to ASTM D 638. Dynamic mechanical properties were evaluated through a temperature sweep method (Mettler Toledo, star system software). The temperature sweep of the testing was -140°C up to +100°C with a constant heating rate of 3 °C/min and at 1 Hz frequency according to ASTM D 4092. Wide-angle XRD analysis was conducted through a PANalytical powder x-ray diffractometer with CuKα radiation, diffraction angle from 5 up to 50°, and a scanning rate of 2 °C/min. The FTIR spectra were taken by a Nicolet iS5 spectrometer with the reflection mode in the range 700 up to 4000 cm^{-1} (Nicolet, SMART Multi-bounce HART). Differential scanning calorimetry (DSC) studies were conducted using the DSC Q100 TA instrument, coupled with a Refrigerated Cooling System (RCS). The calibration in temperature and heat flow is performed using standards like Indium. The experiments were conducted under an inert nitrogen atmosphere with a flow of 50 mL/min. The samples were heated up to 160°C to erase the thermal history, and cooled down to -60 °C at a cooling rate of 10 °C/min. Then, the samples were heated a second time up to 160 °C at a heating rate of 10°C/min. The cooling and the second heating are analyzed in this work. AFM (A-100 SPM, APE Research Nanotechnology, Italy) was used to study the surface morphology of filler and composites. Images were recorded in contact mode using a silicon nitride probe. Nanocomposites' surface morphology and tensile fractured surfaces were performed

on a Zeiss LEO 1530-FESEM. All the samples were coated with a thin film of carbon black prior to Scanning Electron Microscope (SEM) analysis. The morphology and dispersion of fillers in the nanocomposites were analyzed through TEM (JEOL, JEM-2100). Ultrathin sections of Cryo-cut specimens (~100 nm thickness) prepared using an ultramicrotome (Leica, Ultracut UCT) were embedded on a 300 mesh Cu grid. Dielectric spectroscopy measurements were performed using a Wayne Kerr 6500B dielectric instrument. The sample thickness was around 2 mm in all cases. Permittivity was recorded in frequencies ranging from 20 Hz to 30 MHz at room temperature. The silver paste was applied to the front and rear surfaces of the samples. Thermogravimetric analysis (TGA) was carried out using a TGA Discovery instrument from TA INSTRUMENTS. The analyses were carried out under nitrogen (25 mL/min) in the 30-800 °C range, at 10 °C/min scanning rate, on 5-10 mg samples. The thermogram analysis determined the onset degradation temperature (T_{onset}), the temperature corresponding to 5% mass loss, and the final residue at 800 °C.

3. Results and Discussion

3.1. Torque analysis

The torque variations that occurred during the mixing of these composites are represented in Figure 1. The torque vs. time plot (Figure 1) gives the nanocomposites' rheological property and processing superiority. The total value of torque directly reflects the chemical and physical characters and apparent viscosity. Torque versus time plot also gives the degree of uniformity of the mixture. All the compositions showed a similar processing tendency, as noted from the curves (Figure 1). With the addition of cold solid XLPE pellets, the torque shoots up initially. As soon as the melting process initiated, the torque started decreasing, and this trend continued to be the same for all the samples below up to 100 seconds. Upon further mixing, the torque increases due to crosslinking of the XLPE by peroxide present in the compound, and finally, the torque levels off after 400 seconds, indicating a good level of mixing and the completion of the crosslinking process. The addition of the nanofillers increases the torque of all the filled nanocomposites compared to neat XLPE, and 10% fumed SiO_2 nanocomposites showed the maximum torque. After the addition of fumed SiO_2, a sudden increase in torque was observed due to the increased viscosity of the system. Pang *et al*. (2015) reported a similar type of torque

plot in the LLDPE/PVOH blend.[36] The inset plots indicate the weight percentage of fumed SiO_2 versus the maximum and equilibrium torque. Higher SiO_2 loading leads to restricting the free space for the movement of the XLPE matrix and subsequently increases the viscosity of the composites. Composites with 10% fumed SiO_2 showed the highest equilibrium torque value.

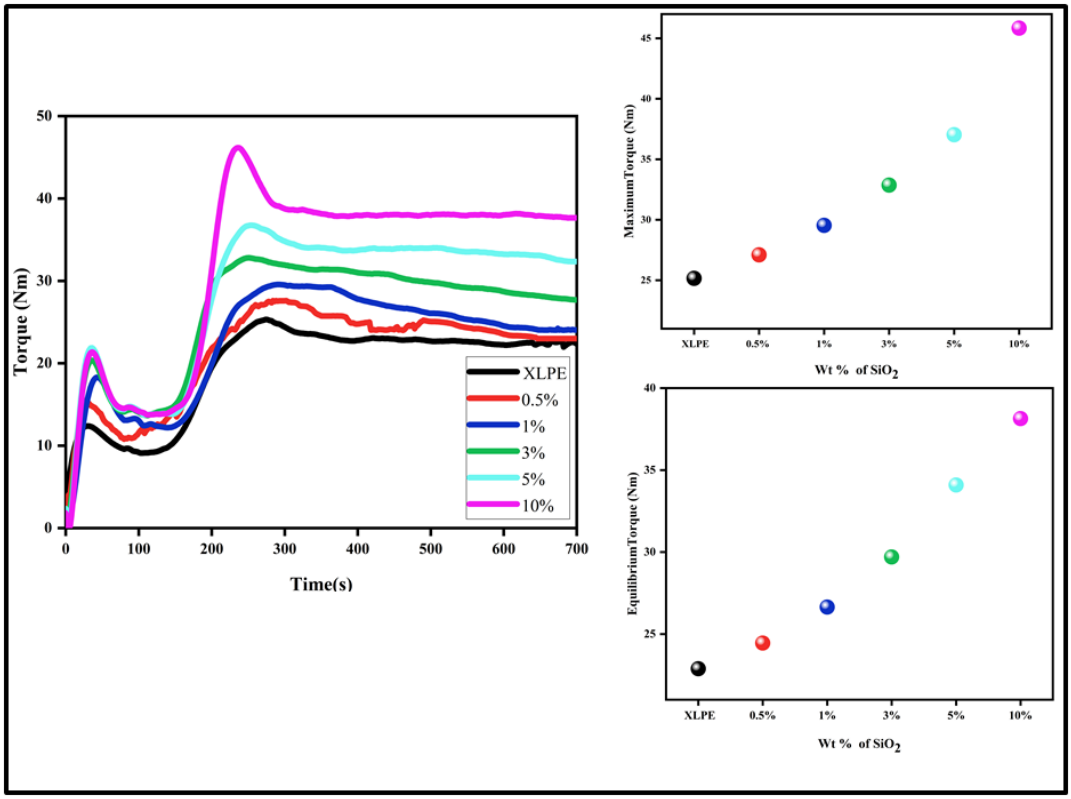

Figure 1: Time versus torque graph of XLPE /fumed SiO_2 nanocomposites

3.2. Structural characterization by FTIR

FTIR spectroscopy is utilized to extract information on the composite material structure. The FTIR spectra are shown in Figure 2. In Figure 2, fumed SiO_2 exhibits the peak at 1020 - 1110 cm^{-1} due to the Si-O-Si asymmetric stretching vibration, and the peak at 800 cm^{-1} is endorsed to the asymmetric bending and stretching vibration of Si-OH,[37] which are not present in XLPE. There is no change in the peak at 2921 cm^{-1}, which indicates the peak of -CH group[38], namely -C-(CH_2)-C-$(n>4)_n$. The peaks at 1463.5 cm^{-1} and 719.7 cm^{-1} are characteristic peaks of the C-H bond in the

crosslinking agents and XLPE/ fumed SiO_2 nanocomposites. The FTIR spectra clearly show the presence of Cab-O-Sil Ts-720 fumed silica in the XLPE matrix.

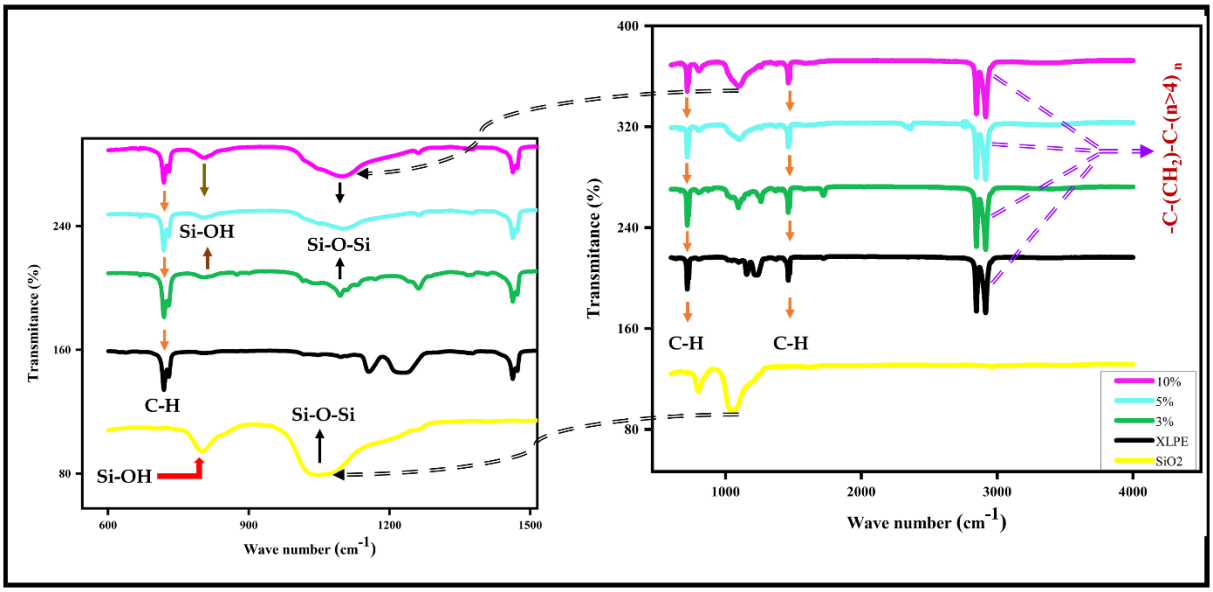

Figure 2: FTIR spectra of XLPE/ fumed SiO_2 nanocomposites.

The broadening of Si-O-Si peaks in the XLPE-fumed SiO_2 nanocomposites is clear evidence for the secondary interactions. Furthermore, there are no additional peaks identified in the FTIR spectra of XLPE nanocomposites other than the peaks of Si-O-Si, C-H, Si-OH, and -C-(CH_2)-C-$(n>4)_n$; this indicates the lack of chemical bonds in the XLPE nanocomposites.

3.3. X-Ray Diffraction analysis

XRD data reveal the amorphous and crystallinity nature of the composite material. Figure 3 shows the XRD pattern of XLPE/ fumed SiO_2 nanocomposites. In Figure 3, the inset plot shows the X-ray Diffraction spectra of fumed SiO_2, and the characteristic diffraction broad peak centered at 21° (2θ) confirmed its amorphous nature. It is clear that by increasing the filler content, the crystal face (110) at 21.61° and (200) peak at 23.81° decreases.[39–41] This is mainly due to the better incorporation of the amorphous nanoparticle into the XLPE matrix. The crystallite size is calculated using with Scherrer formula[42] and is reported in Table 2.

$$D = {}^{0.89\lambda}/_{\beta cos\theta} \quad \text{.....(1)}$$

where D is the crystallite size, β indicates the full width at half-maximum (FWHM), λ the wavelength at 1.5406 nm, and θ symbolizes the Bragg angle.

The crystallinity degree X_c is computed from Eq. 2 and is reported in Table 2.

$$X_c = \frac{I_c}{I_c + I_a} \times 100 \quad \ldots\ldots(2)$$

where Ic, and Ia represent the integrated peak area of the crystalline portion, and the integrated area of the amorphous part, respectively.

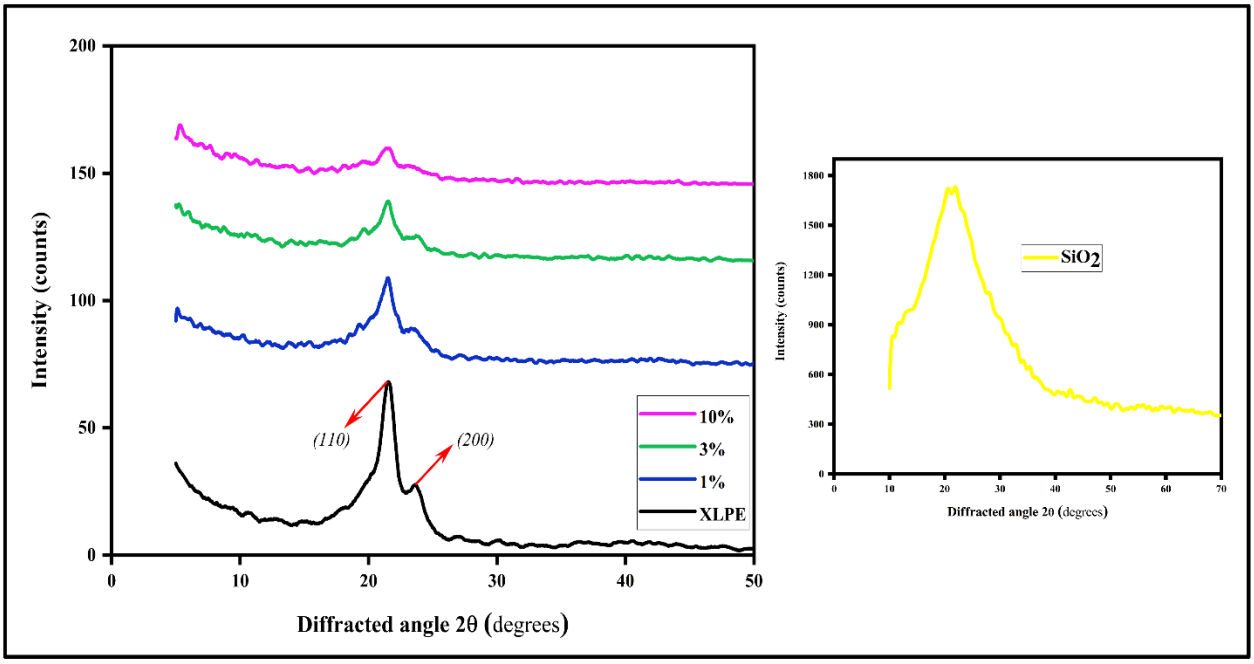

Figure 3: XRD spectrum of XLPE/ fumed SiO_2 nanocomposites

Table 2: Crystallite size D_{size} and Crystallinity degree X_c of XLPE/ fumed SiO_2 nanocomposites

Sample	D_{size} (nm)	Crystallinity degree X_c (%)
XLPE	2.85	44
1%	1.98	38
3%	1.45	34
10%	1.21	30

The crystallinity degree of XLPE/ fumed SiO_2 nanocomposites decreases with the increase of SiO_2 content, and 10% fumed SiO_2/XLPE nanocomposite shows the minimum crystallinity degree (30%). Crystallite size is also related to the crystallinity degree. Here both the crystallite size and the crystallinity degree decrease because of the development of crosslinking, which enhances the amorphous part, reduces the crystalline portion, and also the effects of amorphous nanoparticle–matrix interactions. Noberga *et al*. stated that the crystallinity degree decreases with the formation of crosslinking, which initiates the amorphous portion and reduces the crystalline part.[43]

3.4. Isothermal crystallization from Differential Scanning Calorimeter results

Figure 4 shows the heating (a) and cooling (b) cycles of DSC analyzes of fumed SiO_2-XLPE nanocomposites. The melting and crystallization peak temperature are tabulated in Table 3a. A slight difference in the melting peak temperature and crystallization peak temperature is observed with different concentrations of fumed SiO_2. XLPE shows the melting peak temperature at 110 °C, and the 3% fumed SiO_2-XLPE nanocomposite shows a higher melting peak temperature (113 °C) compared to other systems. The crystallinity degree of fumed SiO_2-XLPE nanocomposites decreases with the addition of fumed SiO_2, and the values obtained from DSC experiments are almost equal to the values obtained from XRD analyses. The lamellar thickness values (Table 3a) of freshly prepared XLPE and its nanocomposites agree with reported values.[41]

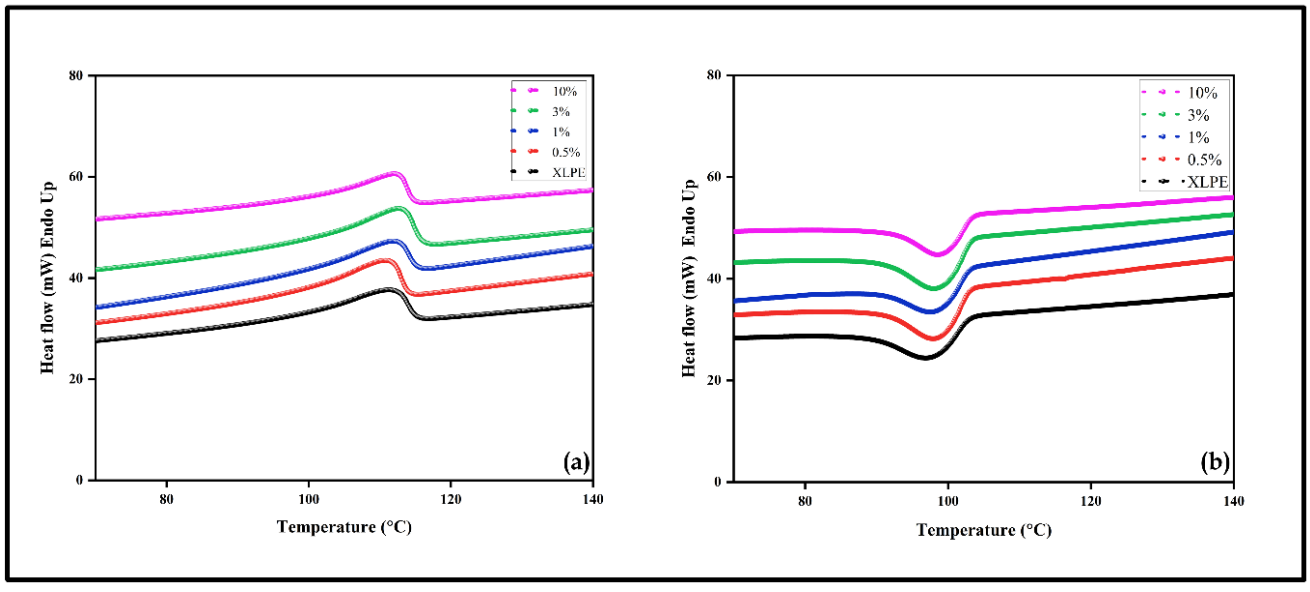

Figure 4: Differential scanning calorimetry analyses of XLPE/ fumed SiO_2 nanocomposites: (a) heating, (b) cooling.

Table 3a: Parameters obtained from DSC (heating and cooling) analyses on XLPE/ fumed SiO_2 nanocomposites

Sample name	**T_m (°C)**	**T_c (°C)**	**ΔT(°C)**	**Crystallinity degree X_c (%)**	**Lamellar thickness (nm)**
XLPE	110	97	13	42	8.28
0.5%	110	98	12	42	8.36
1%	112	98	14	39	9.00
3%	113	99	14	36	9.22
10%	113	99	14	35	9.07

T_m corresponds to the melting peak temperature, T_c to the crystallization peak temperature, $\Delta T = T_m - T_c$ is the degree of supercooling, the crystallinity degree $X_c = \frac{\Delta H_f}{\Delta H_f^0} \times 100$ (%), the lamellar thickness is given by the Gibbs-Thomson equation[41,44]: $T_m = T_m^0 - \frac{2\sigma_e T_m^0}{l \Delta H_f^0}$ where, ΔH_f^0 is the melting enthalpy of an ideal polyethylene crystal per unit volume, ΔH_f is the observed melting enthalpy, T_m is the observed melting temperature (K), T_m^0 is the equilibrium melting temperature of an infinitely thick crystal, σ_e is the bottom and top fold surface free energy, and l is the lamellar thickness. The constant values used for the calculations are $\sigma_e = 93 \times 10^{-3}$ J/m^2 is the well-known value for polyethylene which was obtained from polymer nucleation theory,[45,46] $T_m^0 = 414.6\ K$, $\Delta H_f^0 = 2.93 \times 108\ \mathrm{J/m^3}$ (it is assumed that density for the perfect crystal of polyethylene is 1 g/cm^3).[46,47]

For the calculation of the isothermal crystallization, samples were annealed at annealing temperature (T_a) = 150 °C for 1 min, followed by cooling at a rate of 20 K/min to the respective

crystallization temperature (T_c) (ranging from 100-110 °C) and held until crystallization was complete. The half-time of crystallization ($t_{0.5}$) was determined at $T_c = const$. The same procedure was applied for the determination of the melting temperature. After crystallization, the samples were heated up to 150 °C with a rate of 10 K/min. The kinetics of crystallization for neat XLPE and XLPE-fumed silica nanocomposite were analyzed using Avrami's equation.

$$X(t) = 1 - \exp\left[-K_A^{1/n} t\right]^n \quad \ldots\ldots\ldots\ldots\ldots\ldots\ldots\ldots\ldots\ldots\ldots\ldots\ldots\ldots\ldots\ldots\ldots\ldots\ldots\ldots\ldots(3)$$

Here X(t) is the degree of conversion, defined as the ratio between the crystallinity degree at time *t* and the final crystallinity degree. K_A is the rate of crystallization and *n* the Avrami's exponent (value of *n* depending on the nature of nucleation and the growth dimension).

Table 3b: Avrami's parameters for XLPE-fumed SiO_2 nanocomposites

fumed SiO_2 **(%)**	$t_{0.5}$	n	K_A	r^2
0	1.23	1.84	0.47	0.9996
0.5	1.91	1.91	0.40	0.9996
1	3.03	1.89	0.23	0.9991
3	3.59	2.03	0.19	0.9998
10	4.13	2.16	0.17	0.9982

It can be noticed from Table 3b, the values of *n* (Avrami's exponent) are between 1.8 and 2, indicating the thermal nucleation with two-dimensional crystal growth formation in XLPE- fumed SiO_2 nanocomposites. The crystallization rate (K_A) shows a decreasing trend in the addition of fumed silica, indicating the nucleating behavior of amorphous fumed silica. Thermogravimetric analyses (TGA) of the XLPE nanocomposites are provided in the supporting information (SI) section Fig. S1.

3.5. Morphological study by AFM and TEM

AFM is used to analyze the surface morphology of the nanocomposites. Significant changes in the surface morphology of fumed SiO_2 filled nanocomposites were observed in Figure 5, which could be due to the formation of the higher interfacial area with SiO_2 loading. The roughness of filled nanocomposites was due to the enhanced interfacial adhesion between XLPE and SiO_2 nanoparticles. Focussed ion beam scanning electron images (FIBSEM) of XLPE-fumed SiO_2 nanocomposites confirmed the presence of fumed SiO_2 nanoparticles in the XLPE matrix and are provided in the supporting information (SI) section Fig. S2. Thus, the increase of the mechanical achievement with the filler concentration can be clarified using the theoretical models proposed by Nicolais–Narkis, and Pukanszky.

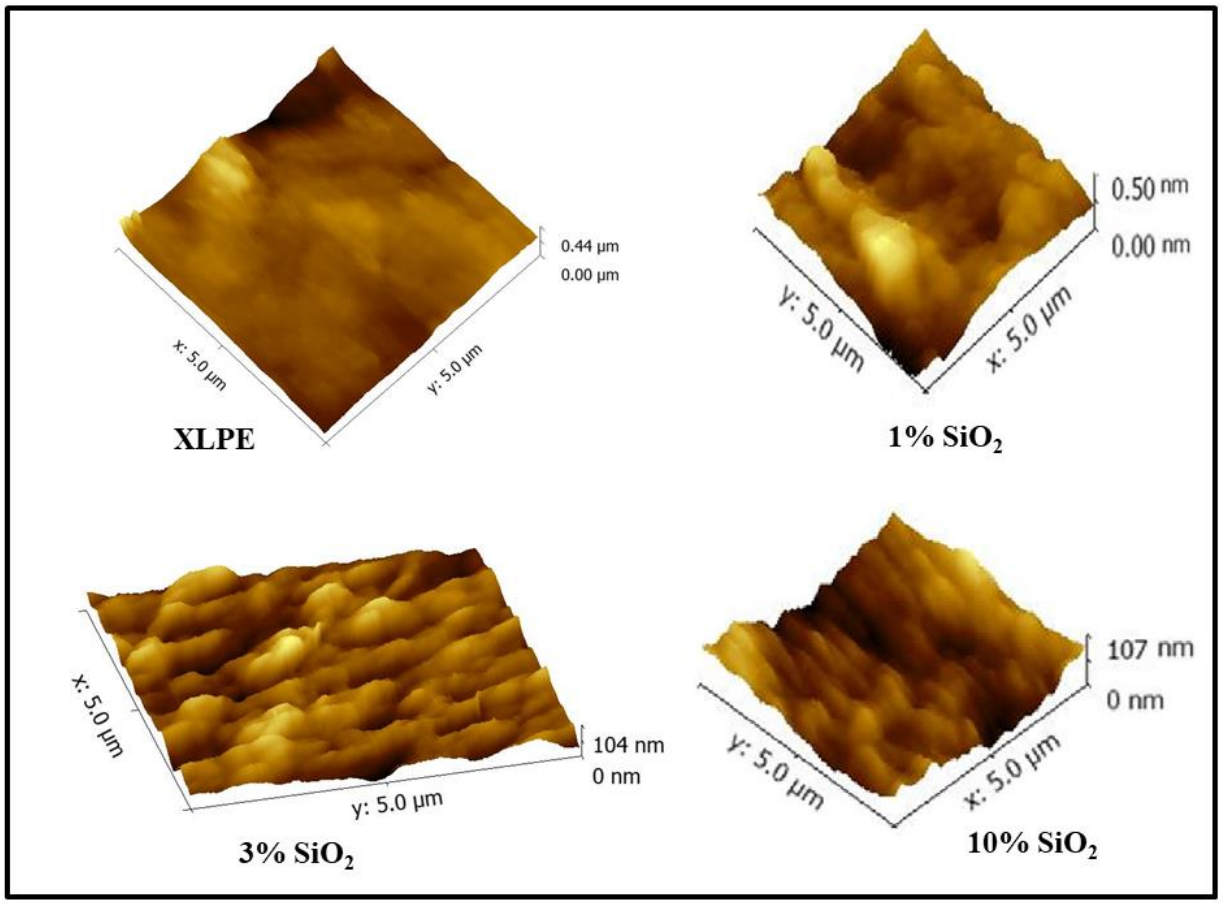

Figure 5: AFM images of fumed SiO_2-XLPE nanocomposites.

TEM images of nanocomposites with different concentrations of fumed SiO_2 nanoparticles are depicted in Figure 6. In 0.5% fumed SiO_2 nanocomposites (lower concentration), the amount of fumed SiO_2 is inadequate to develop a 3D network morphology in the XLPE matrix when the volume of fumed SiO_2 touches at 3%, isolated nanospheres are in interaction with each other, and the number of nanospheres is enough for the expansion of network morphology in XLPE. The inset TEM image 3% fumed SiO_2 shows the network formation of fumed SiO_2 (shown in Figure 6b). The schematic diagram shows the dispersion of fumed SiO_2 and the formation of networks represented in Figure 6c. The fine dispersion of nanospheres in the XLPE matrix is well explained with the models proposed by Nicolais–Narkis, and Pukanszky. However, for higher loading of SiO_2 nanoparticles (10% SiO_2), a well-interrelated network arrangement of SiO_2 is established in the XLPE matrix, but the presence of filler-filler agglomeration reduces the mechanical properties.

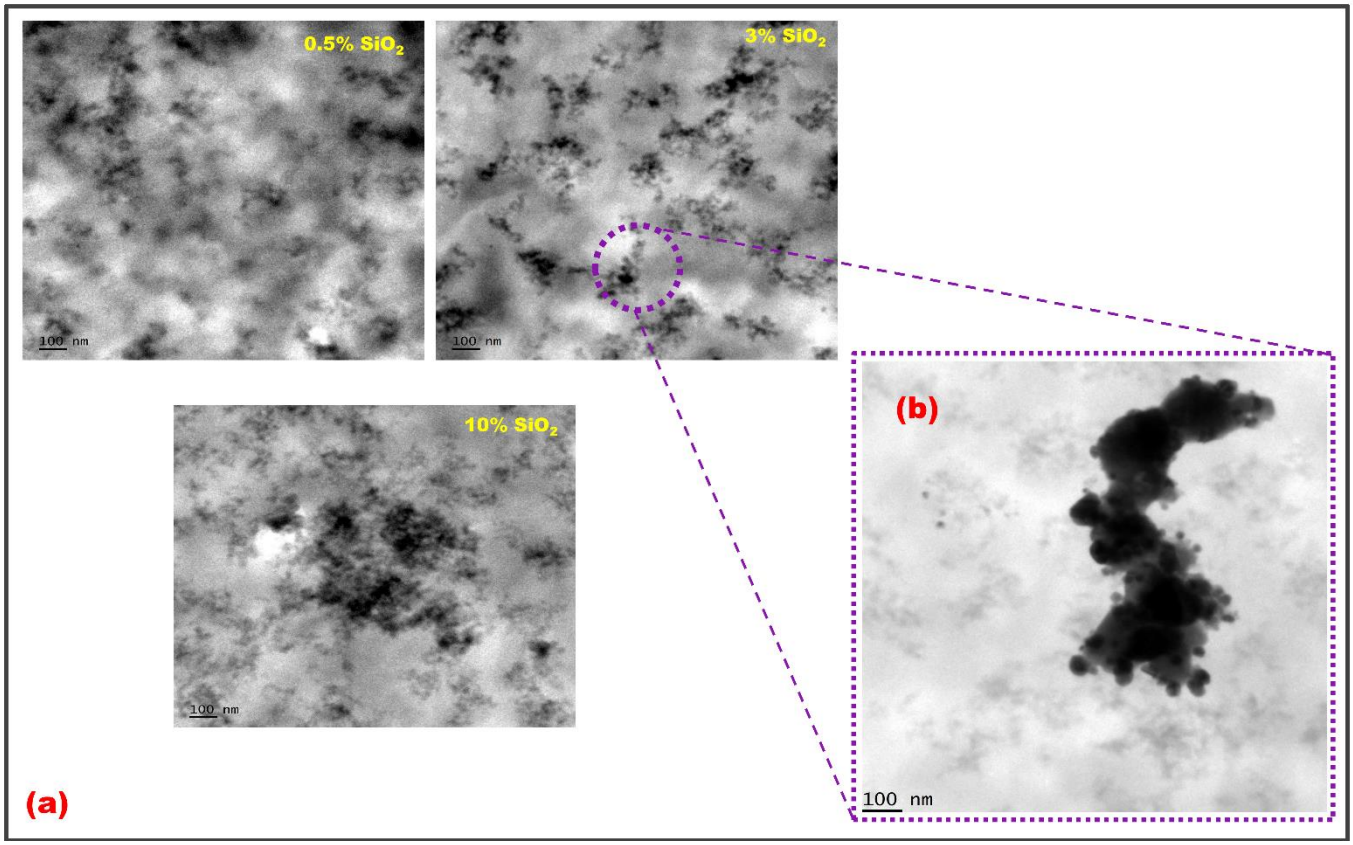
0.5% SiO2
3% SiO2
10% SiO2
100 nm
100 nm
100 nm
(a)
(b)
100 nm

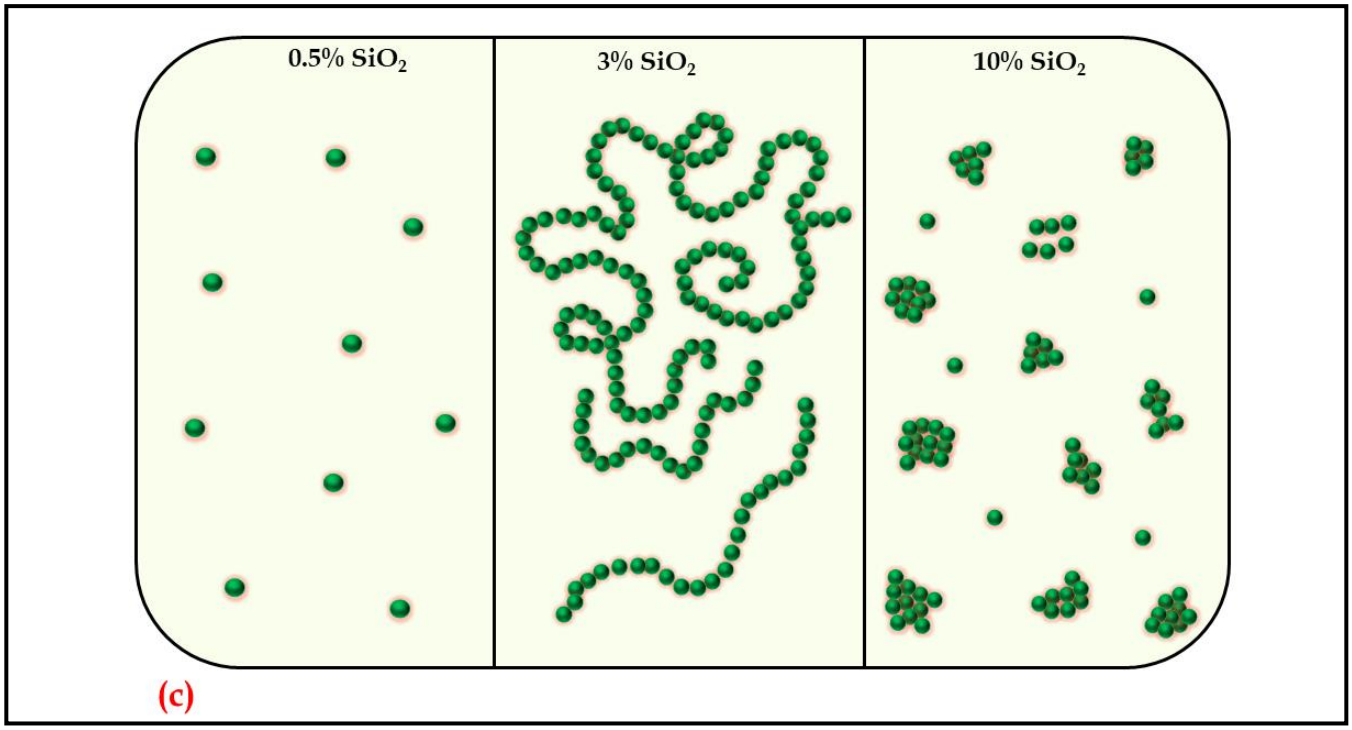
0.5% SiO2
3% SiO2
10% SiO2
(c)

Figure 6: TEM images of fumed SiO_2- XLPE nanocomposites (a) and their schematic representations (c).

3.6. Mechanical Properties

Mechanical properties indicate the interphase adhesion and the interactions in polymer nanocomposites, and the reinforcing impact of nanoparticles. The stress-strain plots of XLPE nanocomposites having 1, 3, 5 and 10wt% fumed SiO_2 are shown in Figure 7a. Observing the stress-strain curves, 3 and 5wt% show higher stress than the other systems, but the highest filler-loaded system, 10wt%, shows a decreasing trend due to higher fumed SiO_2-SiO_2 interactions than XLPE/fumed SiO_2 interactions. As anticipated, tensile strength and modulus of XLPE nanocomposites increase with increasing concentration of fumed SiO_2 at a given strain, and the results show the good incorporation of fumed SiO_2 on the XLPE matrix. There is a gradual increase in tensile strength and Young's modulus of all the samples up to 3wt% of fumed SiO_2. After that, there is a reduction in tensile strength and Young's modulus. This is due to the effect of filler-filler interactions.[48] This enhancement reveals the better reinforcing power of fumed SiO_2 and, thereby strong secondary bond between fumed SiO_2 and the XLPE. Tensile strength values increase with the concentration increasing of fumed SiO_2 and achieve up to 22.1 ± 0.5 MPa (3% fumed SiO_2) from 16.0 ± 1.0 MPa (XLPE). The enhancement in mechanical properties is attributed to (a) the remarkably high strength of nano SiO_2, (b) the improved dispersion of nano SiO_2 in the XLPE matrix by Brabender melt mixing assisting the bonding between polymer and nanospheres. Other mechanical properties like toughness, yield strength, etc., are summarized in Table 4.

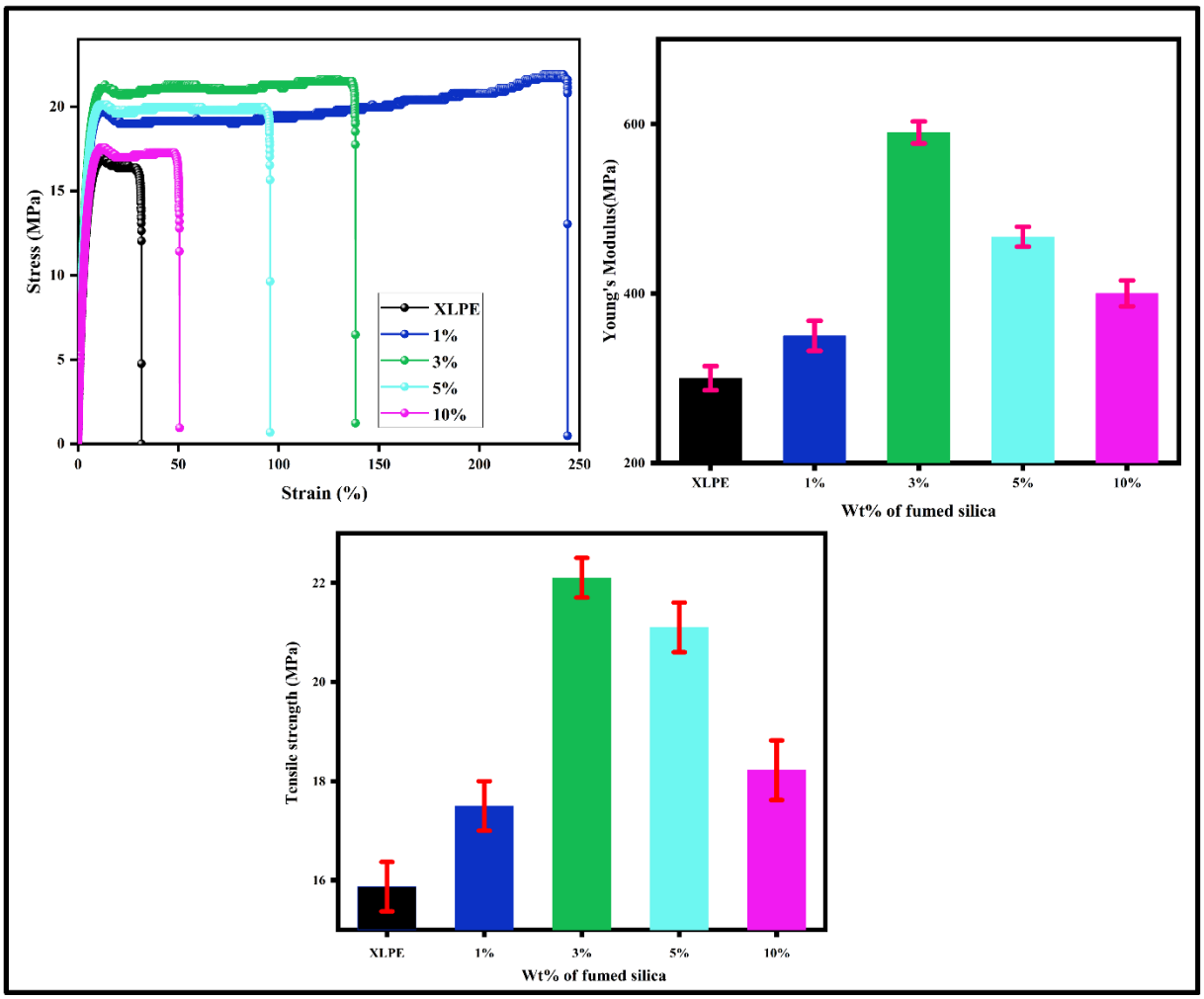

Figure 7a: Stress-strain behavior, tensile strength, and Young's modulus of XLPE/ fumed SiO_2 nanocomposites.

Table 4: Mechanical properties of XLPE/ fumed SiO_2 nanocomposites

Sample	Tensile strength (MPa)	Young's Modulus (MPa)	Elongation at break (%)	Yield strength (MPa)	Toughness (J/M^3)
XLPE	16.0 ± 1.0	300 ± 1	32	16.7 ± 1.0	93940 ± 2
1%	17.5 ± 0.7	350 ± 1	244	19.6 ± 0.5	320992 ± 1
3%	22.1 ± 0.5	590 ± 1	136	21.0 ± 1.5	262821 ± 1
5%	21.1 ± 0.6	467 ± 1	95	20.1 ± 0.7	191225 ± 2
10%	18.2 ± 0.8	400 ± 1	49	17.6 ± 0.4	136432 ± 1

3.6.1. Tensile fracture surface analysis

SEM observations of tensile fractured surfaces of XLPE-fumed SiO_2 nanocomposites are illustrated in Figures 7 b and c. In addition to AFM and TEM analysis, tensile fractured surface micrographs provide the structure-property relationship of XLPE- fumed SiO_2 nanocomposites. It is evident from Figure 7b, XLPE possesses smooth fibrillated morphology due to its higher plastic deformation nature.[49–51] It is noticed that roughness increases with increasing concentration of fumed SiO_2, and maximum roughness was found to be for 10% XLPE- fumed SiO_2 nanocomposite, which supports Figure 5. However, 10% XLPE- fumed SiO_2 nanocomposite has a higher roughness nature which is predominantly due to the filler-filler interactions, which reduce the tensile strength. 10% XLPE- fumed SiO_2 nanocomposite surface has shown flakes, indicating the deterioration of tensile performance and leading to the catastrophic failure of the matrix, and SiO_2 could not participate in the load transfer process due to the lack of interfacial interaction between XLPE and SiO_2. Interfacial parameter (a) for 10% XLPE- fumed SiO2 nanocomposite is lower than that of 3% XLPE-fumed SiO_2 nanocomposite; the lower 'a' value indicates good adhesion between matrix and filler, which was effectively discussed in reinforcement mechanism and theoretical modeling section. In connection with Figure 6, the rough fractured surface of 3% XLPE-fumed SiO_2 nanocomposite indicates the uniform dispersion of SiO_2 in XLPE. Higher magnification SEM image of 3% XLPE-fumed SiO_2 nanocomposites (Figure 7c) illustrated the network forming effect of SiO_2 in the matrix, which was confirmed from TEM images. The

network forming effect of SiO_2 effectively transferred the stress to the entire portion of the matrix, enhancing the nanocomposite's tensile strength. Lower 'a' value for 3% XLPE-fumed SiO_2 nanocomposites due to the enhanced network structure formation of SiO_2 in the XLPE indicates strong interfacial adhesion between XLPE and SiO_2.

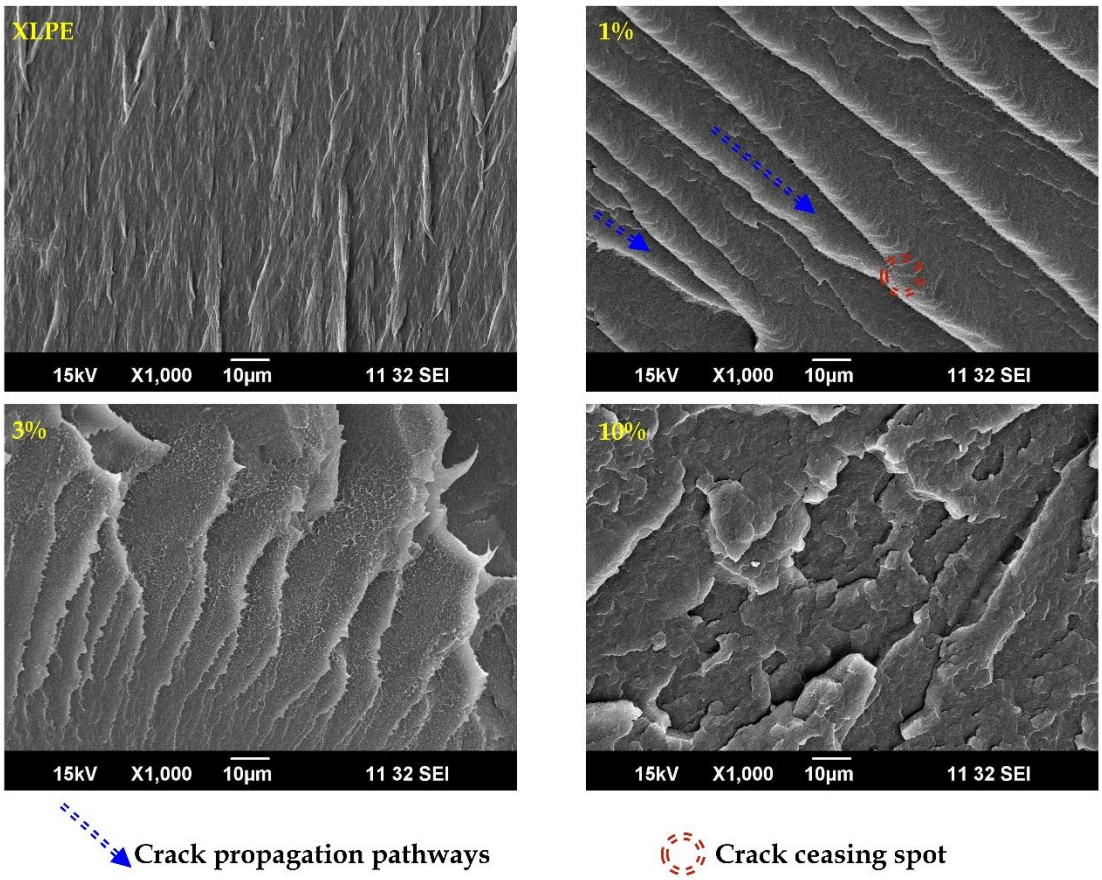

Figure 7b: SEM micrographs of the tensile fractured surface of XLPE/ fumed SiO_2 nanocomposites.

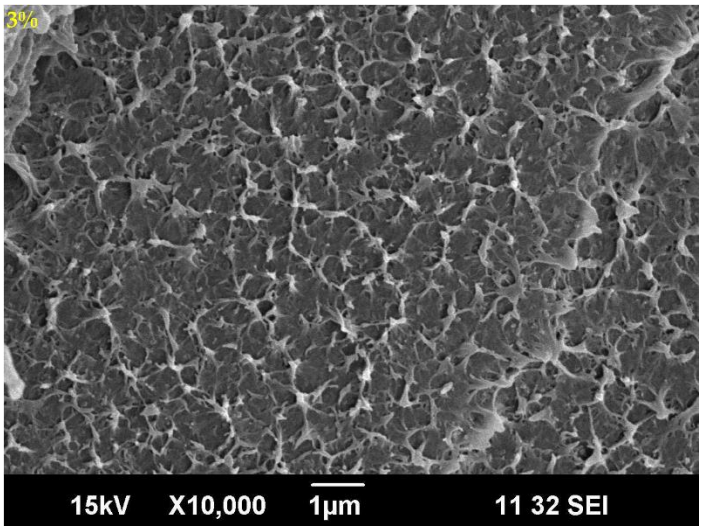

Figure 7c: Higher magnification SEM micrographs of the 3% XLPE/ fumed SiO_2 nanocomposites.

Moreover, the addition of SiO_2 somewhat ceases the crack propagation pathways was seen in 1% of the nanocomposite. In 3% nanocomposite, the crack pathways were almost ceased due to the strong interaction between XLPE and SiO_2. The high crack propagation rate resulted in the formation of flakes surfaces in 10% nanocomposite due to the agglomeration of SiO_2 and poor interfacial adhesion between matrix and nanoparticles.

3.7. Reinforcement mechanism and theoretical modeling

Several micromechanical theoretical studies on the interfacial/ interphase area have contributed an ample amount of data that favors the attainment of expected mechanical properties like yield strength, Young's modulus, tensile strength, etc. Pukanszky[29] established an easy model connecting the yield strength of polymer composites to interfacial parameters, and it was successfully applied in various polymer nanocomposites.[47,52–55] Here, we successfully applied this model in SiO_2–XLPE nanocomposites for predicting interfacial properties. In this Pukanszky's model, 'B' is the interfacial parameter; it indicates the capability of stress transfer from the polymer matrix to the nanoparticle, as a function of the particle density and specific surface area, thickness, and strength of interphase.[56] The Pukanszky's model for the yield strength of composites is presented as:

$$\sigma_R = \frac{1-\phi}{1+2.5\phi} exp\ (B\phi) \quad \text{.....(4)}$$

where, 'σ_R' indicates the relative yield strength as $\sigma_R = {}^{\sigma_c}/_{\sigma_m}$, 'σ_c' and 'σ_m' represent the yield strengths of composite and matrix, respectively.

The term $\frac{1-\phi}{1+2.5\phi}$ displays the cut of an effective load-bearing cross-section through filler inclusion.

$$B = \left(1 + A_c \rho_f t_i\right) \ln\left(\frac{\sigma_i}{\sigma_m}\right) \quad \text{.....(5)}$$

where 'A_c' denotes the surface area of nanofiller, 'ρ_f' is the nanofiller density, 't_i' and 'σ_i' are the thickness and strength of interphase, respectively. Nanocomposites containing spherical particles 'A_c' become,

$$A_c = \frac{A}{m} = \frac{A}{\rho_f \vartheta} = \frac{4\pi r^2}{\rho_f \frac{4}{3}\pi r^3} = \frac{3}{\rho_f r} \quad \text{.....(6)}$$

where '*A*,' '*m*', '*v*' and '*r*' are surface area, mass, volume, and radius of nanoparticles, respectively.

Then the Eq. (5) become

$$B = 1 + 3\frac{t_i}{r} \ln\left(\frac{\sigma_i}{\sigma_m}\right) \quad \text{.....(7)}$$

By rearranging Eq.(7), 't_i' is calculated by:

$$t_i = r\left[\frac{B}{3\ln\left(\frac{\sigma_i}{\sigma_m}\right)} - \frac{1}{3}\right] \quad \text{.....(8)}$$

r = 26 nm, obtained from TEM analysis.

Leidner-Woodhams[57] developed a model to compute the interphase yield strength for polymer nanocomposites as:

$$\sigma_c = \left(\sigma_i + 0.83\,\frac{\sigma_m}{\sqrt{3}}\right)\phi_f - \sigma_i \frac{1}{B}\,\phi_m + \sigma_i \frac{1}{B} + \sigma_m \quad \text{.....(9)}$$

where 'σ_i' is the interphase strength of the polymer composites.

By rearranging of Eq. (5), 'σ_i' stated as a function of volume fraction of nanofiller (ϕ_f) as:

$$\sigma_i = \frac{\sigma_c - \sigma_m - \left(0.83\,\frac{\sigma_m}{\sqrt{3}}\right)\phi_f}{\left(1+\frac{1}{B}\right)\phi_f} \quad \text{.....(10)}$$

The adhesion factor 'a' is calculated from Nicolais–Narkis's[58] model for yield strength and is given below

$\sigma_R = 1 - a\phi^{2/3}$ ……..…….…….....(11)

where 'a' indicates the interfacial parameter, which explains the properties of the interphase/interface. The value of 'a' is below 1.21, indicating a good adhesion.

Using Eqs. (4), (8), (10), and (11) the parameters 'B', 'σ_i,' 'a', and 't_i' are calculated from the experimental results and are tabulated in Table 5.

Table 5: The characteristics and interphase calculations of the XLPE/fumed SiO_2 nanocomposites

Fumed SiO_2 wt%	Vol. fraction of fumed SiO_2	σ_R (MPa)	σ_i (MPa)	B	a	t_i (nm)
1	0.004	1.09	6.75	24.89	-2.50	62.12
3	0.012	1.35	9.72	28.03	-4.95	45.42
5	0.020	1.29	9.18	16.05	-3.03	47.03
10	0.040	1.15	8.25	7.01	-1.07	56.23

At the initial stage, we placed the experimental data of XLPE/ fumed SiO_2 nanocomposites in the Pukanszky's model (Eq. (4)), subsequently 'a' is computed by fitting the experimental results of yield strength to Nicolais–Narkis's model (Eq. (11)). The highest interfacial parameter 'B' value corresponds to the best nanocomposite. Indeed, the higher the 'B' value, the higher the interactions, which implies better mechanical properties. The 'a' value is a measure of the adhesion between matrix and filler; 'a' value below 1.21 indicates good adhesion.[58] From the Table 5, it is observed that all the 'a' values are below 1.21 and maximum decrease is observed for 3 wt% silica content. The values of 'B' and 'a' predict maximum mechanical properties for 3% SiO_2, which is according to the experimental results shown in Figure 7. The decrease in the value of 'B' above 3 wt% fumed SiO_2 can be attributed to the agglomeration of nanoparticles. TEM experiments in Figure 6 clearly show this nanoparticle agglomeration.

Figure 8 shows the effect of the volume fraction of nanofiller on 'B' and 'σ_i' parameters and contour plots of fumed SiO_2-XLPE nanocomposites. 3% fumed SiO_2-XLPE nanocomposite shows higher 'B' and 'σi' values according to the graph.

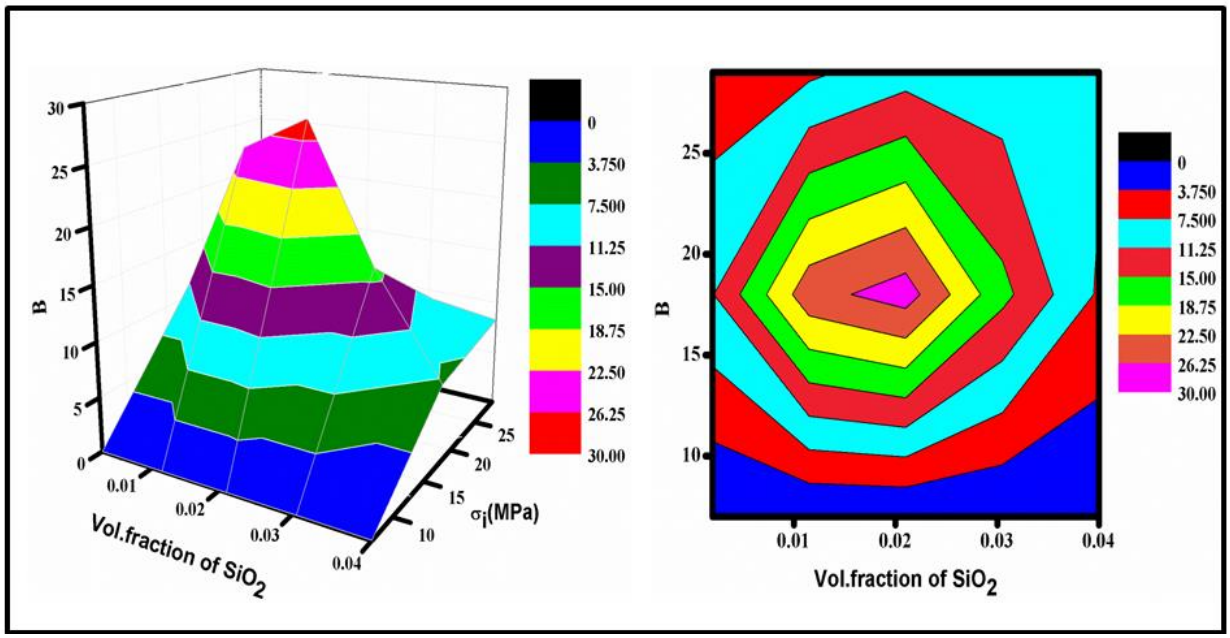

Figure 8: The effect of the nanofiller volume fraction on 'B' and 'σ_i' parameters, and the contour plots of fumed SiO_2/ XLPE nanocomposites

The 'B' parameter depends on the nanofiller dispersion, thickness, and strength of interphase 'σ_i.' The value 'σ_i' increases with increasing 'B' value, and it is found that 'σ_i' value is higher in 3% fumed SiO_2/ XLPE nanocomposite, due to better interactions of filler and matrix. Figure 9 indicates the relation between the three parameters, namely 'B,' 'a' and 'σ_R' in fumed SiO_2/ XLPE nanocomposites. The 't_i' and 'σ_i' exhibit inverse relations in polymer nanocomposites, i.e., the thicker interphase shows lower 'σ_i,' and thinner interphase will be a stronger due to the higher 'σ_i.'

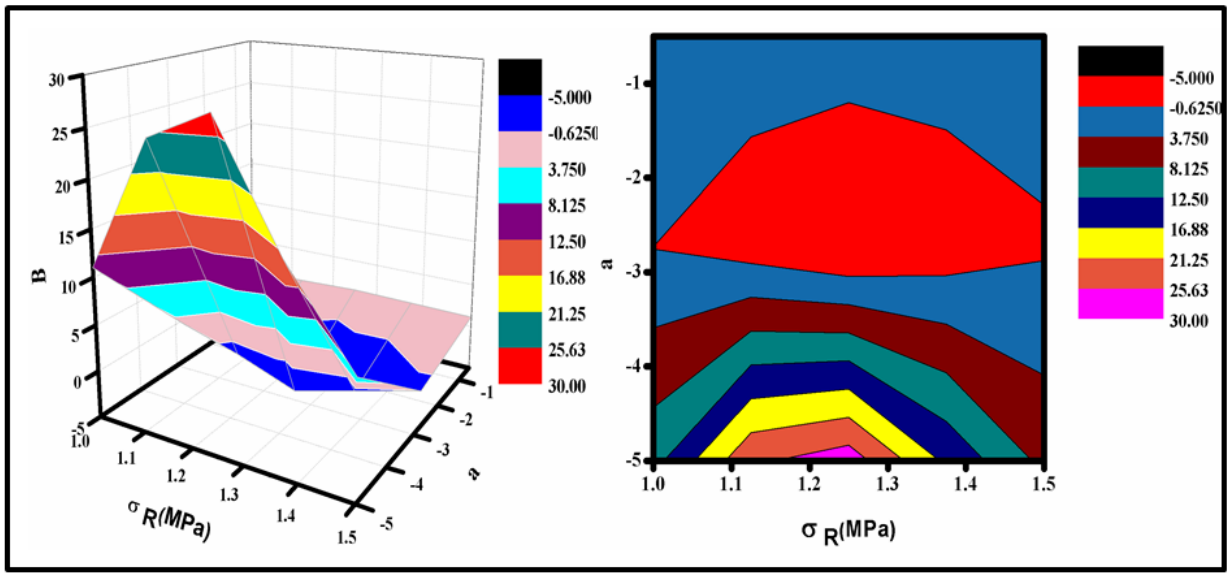

Figure 9: The relation between 'B,' 'a' and 'σ_R' and their contour plots of fumed SiO_2/ XLPE nanocomposites

3.8. Dynamic mechanical analysis

The dynamic mechanical analysis has been performed to acquire filler loading and temperature information on the storage modulus and loss modulus of neat XLPE and its nanocomposites (shown in Figure 10A-B). With the addition of fumed SiO_2, the storage modulus of XLPE nanocomposites displayed greater values than that of neat XLPE.

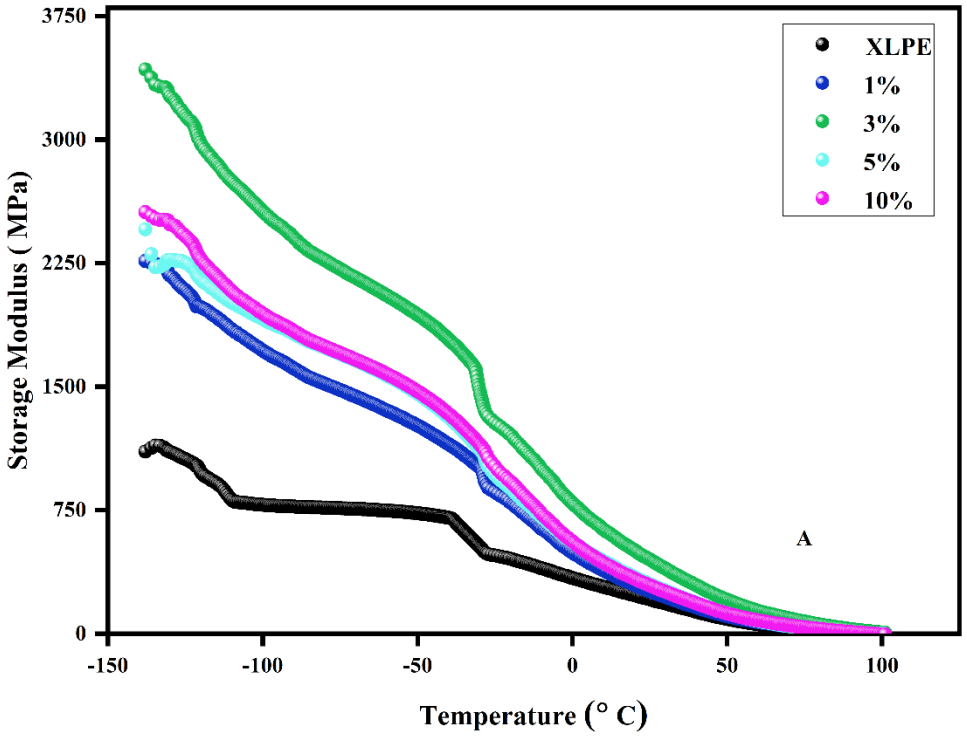

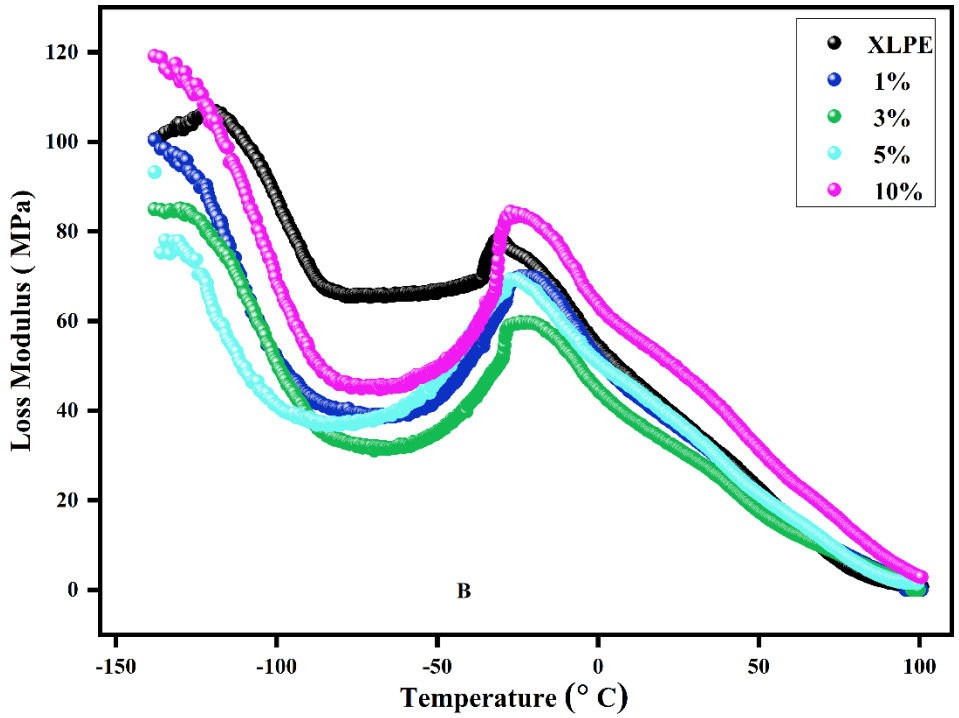

Figure 10 (A) Storage modulus, **(B)** loss modulus of pure XLPE and its nanocomposites with respect to temperature.

It is noted that incorporating fumed SiO_2 produced an upturn in storage modulus values over the entire temperature range, with the highest modulus for the 3wt% fumed SiO_2/XLPE nanocomposite. It upturns dramatically up to 3261 MPa (at -123.15 °C) in the glassy region, which is three times larger than that (1102 MPa) of neat XLPE, demonstrating that the nanofillers are evenly distributed and have solid interfacial adhesion with the matrix. The prominent enhancement in storage modulus by the addition of fumed SiO_2 clearly demonstrates strong confinement effect or interface interactions between fumed SiO_2 and XLPE chains and high restriction of polymer chain mobility by the adsorption of polymer segments on the surface of nanofillers.[59,60] The improved interfacial adhesion in 3wt% fumed SiO_2 / XLPE nanocomposite facilitates higher stress transfer between the fumed SiO_2 and the matrix. In these circumstances, reinforcement executes the stable constrained region in the polymer segments. The filler can share the load from the matrix, thereby boosting its mechanics. Loss modulus as a function of temperature for different XLPE nanocomposites are displayed in Figure 10B. Except for the 10wt% fumed SiO_2 sample, all the composites gives a lower value for loss modulus than neat XLPE. The higher loss modulus value suggests the extreme heat initiation within the polymeric composite system by particle-particle interactions as suggested by Nielsen and Landrel.[24]

3.9.1. Effectiveness of nanofiller and Degree of entanglement

The effectiveness of the nanofiller on the modulus of the composites (β_f) is calculated using the equation

$$\beta_f = \frac{\left(E'_g/E'_r\right)_{composite}}{\left(E'_g/E'_r\right)_{pure}} \quad \text{..... (12)}$$

where E'_g represents the storage modulus in the glassy region (150 K) while E'_r is the storage modulus in the rubbery regions (300 K). The lower β_f value indicates the excellent effectiveness of the filler dispersion in the polymer matrix.

Fumed SiO_2 nanoparticles lead to form entanglements in the XLPE matrix. These entangled networks can restrict the free movement of polymer strings, leading to the confinement effect. The degree of entanglement is calculated as:

$$N = \frac{E'}{RT} \quad \text{..... (13)}$$

where 'E'' denotes the storage modulus in the rubbery region (at 300 K), 'R' is the universal gas constant, and 'T' is the absolute temperature at the Kelvin scale.

Table 6: Effectiveness of dispersion, Degree of entanglement of fumed SiO_2/ XLPE nanocomposites

Fumed SiO_2 wt%	Coefficient of Effectiveness (β_f)	Degree of entanglement
1	1.584	0.108
3	1.372	0.187
5	1.417	0.126
10	1.601	0.122

Table 6 gives the values of the effectiveness of dispersion and degree of entanglement of XLPE nanocomposites. The minimum value of 'β_f' indicates the higher effectiveness of the filler. Following conclusions can be made by analyzing the data in Table 6. The effectiveness of filler shows an increasing trend, and the maximum effectiveness (corresponding to an increase for β_f value) is shown by composites loaded with 3wt% fumed SiO_2. A decreasing trend is observed because of the agglomeration of nanoparticles in the polymer matrix. The greater effectiveness of the 3wt% loaded sample is because of the improved, reinforcing effect of filler and the better load transfer between filler and matrix at this composition. This result can be correlated with superior tensile strength and modulus obtained for this composition. The degree of entanglement showed an increasing trend up to 3wt% fumed SiO_2, followed by a decreasing trend. The decrement in entanglement density after this concentration is because of the increased fumed SiO_2-SiO_2

interactions over fumed SiO_2-XLPE interaction. Moreover, in the rubbery region, the mobility of polymer chains is enhanced, so the nanoparticles have a prominent role in enhancing mechanical characteristics.

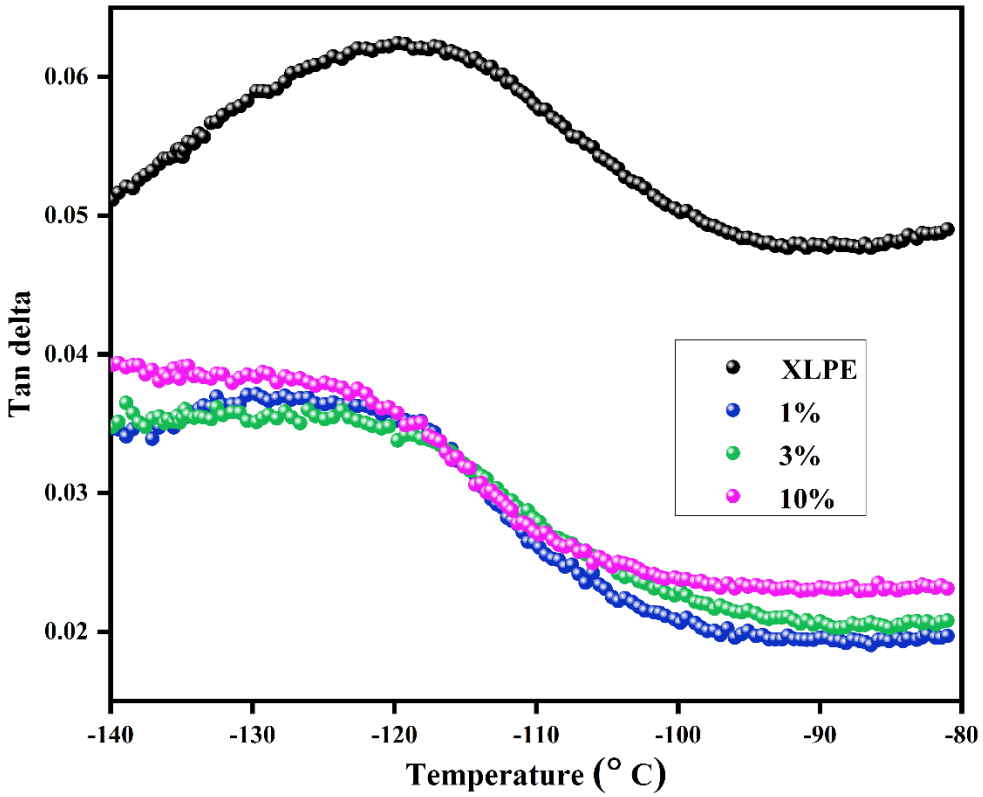

Figure 11a: Tan delta curves of fumed SiO_2- XLPE nanocomposites

The introduction of nanofillers in the polymer matrix leads to the development of an immobilized nanoscopic polymer chain on the filler surface. This glassy polymer layer diminishes the inherent motion of the polymer chains. Constraints implemented on the amorphous phase by crosslinking, molecular packing, free volume, and crystallinity are the various factors that affect the glass transition temperature of a polymer.[61] Figure 11a shows the addition of fumed SiO_2 reduces tan δ peak height in fumed SiO_2-XLPE nanocomposites. The drop in the tan δ peak height reveals that there is restricted mobility of XLPE chains in the presence of fumed SiO_2. A schematic model for the constrained region in the XLPE systems is shown in Figure 11b. The network forming effect of fumed SiO_2 connects with XLPE through non-covalent interactions and disperses uniformly in the XLPE matrix. It is considered that there are 'constrained regions' in the nanocomposite, which are composed of SiO_2, constrained XLPE chains, and peroxide crosslinks.

The volume of constrained chains is calculated from this reduction in peak height.[62] For linear viscoelastic behavior, the energy loss fraction of the polymer nanocomposite 'W' is related to tan δ by the following equation.[63]

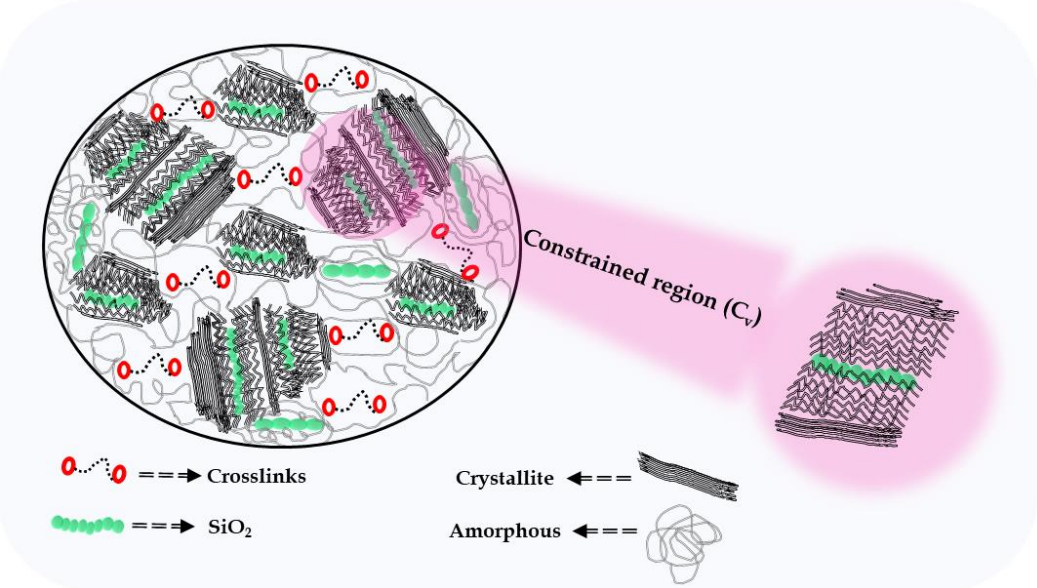

Figure 11b: Schematic representation of the constrained region in the fumed SiO_2-XLPE nanocomposites

$$W = \frac{\pi \tan \delta}{\pi \tan \delta + 1} \quad \text{..... (14)}$$

The following equation gives the energy loss fraction 'W' at the tan δ peak

$$W = \frac{(1 - C_v) W_0}{1 - C_0} \quad \text{..... (15)}$$

where C_v is the volume fraction of the constrained region, $(1 - C_v)$ is the fraction of the amorphous region, and W_0 and C_0 represent the energy fraction loss and volume fraction of the constrained region for pure XLPE, respectively. The volume fraction of the constrained region C_v of the nanocomposites are calculated using equation (15) and are tabulated in Table 7. Homogeneous dispersion of fillers and the good interfacial interaction between fumed SiO_2 and XLPE matrix leads to forming a large constrained region. The XRD spectrum of 3% nanocomposite (Figure 3) indicates the retaining of moderate crystallinity even with the addition of SiO_2. The moderate crystallinity helps form an extensive SiO_2 network in the XLPE matrix, which enhances the

volume of the constrained region is maximum for composites containing 3wt% fumed SiO_2 nanocomposite. At higher filler loading volume of the constrained region is reduced due to the agglomeration of fillers. Furthermore, the excessive content of SiO_2 completely reduces the sharp peak in the XRD spectrum of 10% nanocomposite. It diminishes the matrix's crystallinity, which supports the reduction of the constrained region in 10% nanocomposite.

Table 7: The constrained region volumes of fumed SiO_2-XLPE nanocomposites

Composite	Constrained region (C_v)
XLPE	-
1%	0.628
3%	0.6840
10%	0.5908

3.9. Dielectric Properties

The values of the dielectric constants of XLPE and fumed SiO_2 nanocomposites are shown in Figure 12. We can observe a decrease of dielectric constants from 3.7 (XLPE) to 2.4 (3wt% fumed SiO_2 nanocomposite). With 5 and 10wt%, we observe an increase from 2.7 to 3. The higher value obtained in the case of 10wt% fumed SiO_2 nanocomposite compared to 3 and 5wt% fumed SiO_2 nanocomposites is primarily due to the agglomeration effect of fumed SiO_2 nanoparticles in XLPE matrix, and also the meager interphase interaction between the nanofillers and matrix as observed by TEM. For insulation, the low value of dielectric constant material has many advantages in cable insulation. The highlighted observation of this study is the reduction in dielectric constant for 3 wt% fumed SiO_2 nanocomposite and the invariance of the dielectric constant values with increasing frequency. The invariance of the dielectric constant values with increasing frequency is due to the typical characteristic of non-polar polymers. XLPE is a non-polar material, the polarization of electron displacement arises mainly in its interior, and at the same moment, it does not vary with the frequency. When SiO_2 particles are added to XLPE, they will form many interfaces in the XLPE nanocomposites. The electrical fields change gradually faster when

increasing the frequency; therefore, the relaxation polarization is too slow to keep abreast of the electrical fields.[64,65] In addition to the interface formations, SiO_2 was effectively trapped in the XLPE matrix, forming a well-established network structure in XLPE nanocomposites, as shown in Figures 6b and 7c. Four basic polarization mechanisms exist in response to the applied electric field, i.e., interface polarization, electronic polarization, ionic polarization, and orientation polarization. These polarizations have different activation and ceasing frequencies; therefore, the invariance of the dielectric properties with increasing frequency depends on the nature of materials and their polarization.[66]Although polymers like polyoxafluoronorbornene,[67] epoxy,[68], etc., show the dielectric's invariance with increasing frequency.

The drop in dielectric constant value mainly depends on the polymer chain mobility and filler loading. The decreased rate of polymer chain flexibility in the XLPE/ fumed SiO_2 nanocomposites is due to the physicochemical bonding of XLPE and fumed SiO_2 nanoparticles. Several studies imply that some nanometric dimensions were helpful in the creation of the chain entanglement, which could have a considerable effect on the interaction zone.[69–72] As the nanofillers have a high specific surface area, the interaction area will be more prominent, and it impedes the polymeric chain flexibility, which further directs to the slashing of the dielectric constant.[73–75]

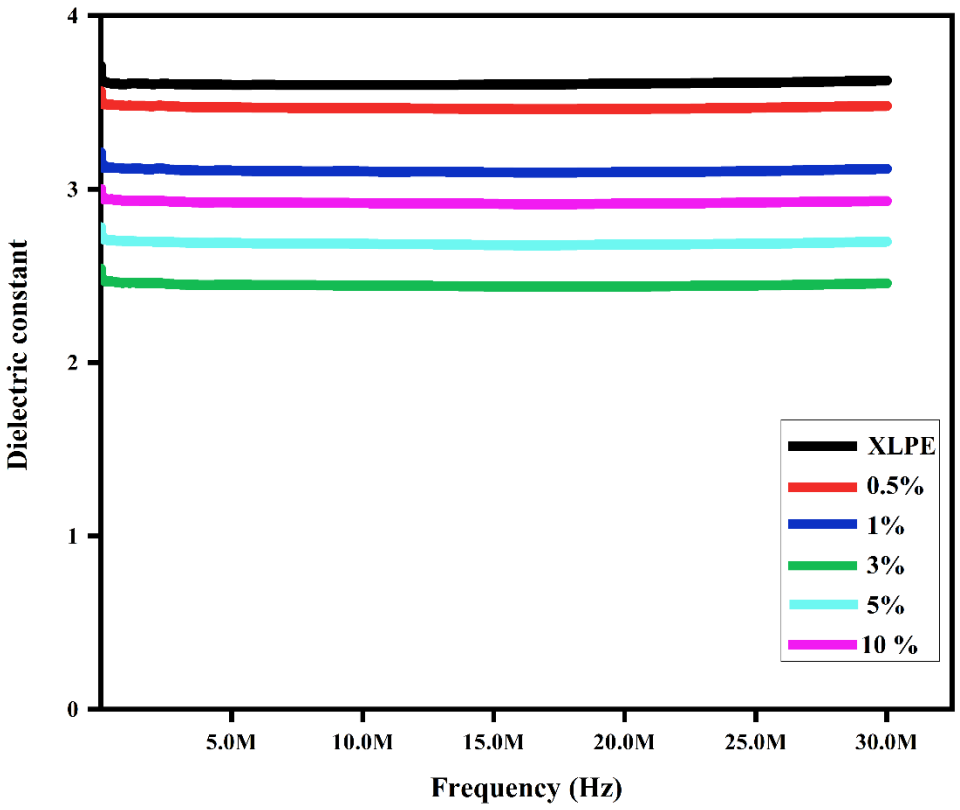

Figure 12: Dielectric constant of XLPE/ fumed SiO_2 nanocomposites ('M' stands for mega=10^6)

4. Conclusions

A systematic analysis has been made on the structural, thermal, morphological, and mechanical properties of fumed SiO_2-XLPE nanocomposites in this work. This study unlocks a new pathway for interface analysis on XLPE nanocomposites via the models of Nicolais–Narkis and Pukanszky. The interphase characteristics and interfacial properties of XLPE nanocomposites have not been explored so far. Our study is the first in this direction. Therefore, our findings and approaches for the fabrication of mechanically robust XLPE systems are beneficial for the HVDC (high voltage direct current) and HVAC (high voltage alternating current) cable applications. The mixing torque analysis confirmed all the compositions showing a similar tendency of processing torque curves are perceived, and nanocomposites with 10% fumed SiO_2 showed the highest equilibrium torque due to the higher viscosity of the system. The FTIR spectra of fumed SiO_2-XLPE nanocomposites indicate the presence of asymmetric stretching vibrations of Si-O-Si at 1020 - 1110 cm^{-1}, and the peak at 800 cm^{-1} is endorsed to the asymmetric bending and stretching vibration of Si-OH.

The XRD analysis reveals the reduction of the crystallinity degree and the crystallite size with the addition of fumed SiO_2. Decreases in crystallinity degree of fumed SiO_2-XLPE nanocomposites were confirmed by DSC analysis. Superior static and dynamic mechanical performance could be supported by the microstructural developments in the XLPE matrix as verified from microscopic techniques. The experimental results of mechanical characterizations are in good agreement with the theoretical models of Nicolais–Narkis, and Pukanszky. The fabricated nanocomposites demonstrate a better storage modulus than XLPE, particularly at low temperatures, given the reinforcing effect of nanoparticles on the XLPE matrix. The effectiveness of nanofiller and entanglement density has been estimated to get more profound knowledge on the reinforcing mechanism of fumed silica. The amount of XLPE chains confined at the fumed SiO_2 nanoparticles were calculated and quantified using the results attained from the tan delta curves of DMA analysis. 3% fumed SiO_2-XLPE nanocomposites showed maximum volume fraction of constrained region. The dielectric constant studies prove that 3% of fumed SiO_2 nanocomposites can be used in cable insulation fields.

The incorporation of theoretical modeling removes the discrepancies in the observed physical properties of polymer materials. In addition, theoretical studies are a timeless and cost-effective tool that correlates, understands, and predicts physical and chemical properties and gives new research insights. Unfortunately, only a handful of works correlate theoretical modeling with the physical properties of XLPE based materials for cable insulation. By this present work, we recognized the importance of synergy between the theory and the experiments in XLPE based materials, and this work will be a breakthrough for such studies in XLPE materials for cable insulations.

5. Acknowledgments

Allisson Saiter-Fourcin and Bindu Patanair are grateful to the European Union and the Normandy Region for the financial support given to the MAGMA project via the “Fonds Européen de Développement Régional” (FEDER). Allisson Saiter-Fourcin and Bindu Patanair are also acknowledged for Emmanuel Cadel and Fabien Cuvilly. Jince Thomas acknowledges to Mahatma Gandhi University for a university junior research fellowship.

6. References

1. Ouyang, Y.; Mauri, M.; Pourrahimi, A. M.; Östergren, I.; Lund, A.; Gkourmpis, T.; Prieto, O.; Xu, X.; Hagstrand, P.-O.; Müller, C. *ACS Appl. Polym. Mater.* **2020**, *2*, 2389.

2. Gao, Y.; Huang, X.; Min, D.; Li, S.; Jiang, P. *ACS Sustain. Chem. Eng.* **2019**, *7*, 513.

3. Song, S.; Zhao, H.; Zheng, X.; Zhang, H.; Liu, Y.; Wang, Y.; Han, B. *R. Soc. Open Sci.* **2018**, *5*.

4. Pourrahimi, A. M.; Pallon, L. K. H.; Liu, D.; Hoang, T. A.; Gubanski, S.; Hedenqvist, M. S.; Olsson, R. T.; Gedde, U. W. *ACS Appl. Mater. Interfaces* **2016**, *8*, 14824.

5. Wang, W.; Sonoda, K.; Yoshida, S.; Takada, T.; Tanaka, Y.; Kurihara, T. *IEEE Trans. Dielectr. Electr. Insul.* **2018**, *25*, 94.

6. Merati Shirazi, A. H.; Hosseini, S. M. H. *Eng. Fail. Anal.* **2018**, *90*, 262.

7. Thomas, J.; Joseph, B.; Jose, J. P.; Maria, H. J.; Main, P.; Ali Rahman, A.; Francis, B.; Ahmad, Z.; Thomas, S. Recent Advances in Crosslinked Polyethylene-based Nanocomposites for High Voltage Engineering Applications: A Critical Review. *Ind. Eng. Chem. Res.* **2019**, *58*, 20863–20879.

8. Andersson, M. G.; Hynynen, J.; Andersson, M. R.; Englund, V.; Hagstrand, P. O.; Gkourmpis, T.; Müller, C. *ACS Macro Lett.* **2017**, *6*, 78.

9. Walker, R. C.; Hamedi, H.; Woodward, W. H. H.; Rajagopalan, R.; Lanagan, M. In *ACS Symposium Series*; **2021**; pp 239.

10. Liu, S.; Fifield, L. S.; Bowler, N. *Radiat. Phys. Chem.* **2021**, *185*, 109486.

11. Zhou, X.; Yang, J.; Gu, Z.; Wei, Y.; Li, G.; Hao, C.; Lei, Q. *Adv. Eng. Mater.* **2021**, 2100008.

12. XU, A.; ROLAND, S.; COLIN, X. *Polym. Degrad. Stab.* **2021**, 109597.

13. Wang, S. In *Polymer Insulation Applied for HVDC Transmission*; Springer Singapore,

2021; pp 3.

14. Hedir, A.; Moudoud, M.; Lamrous, O.; Rondot, S.; Jbara, O.; Dony, P. *J. Appl. Polym. Sci.* **2020**, *137*, 48575.

15. Zong, R.; Wang, Z.; Liu, N.; Hu, Y.; Liao, G. *J. Appl. Polym. Sci.* **2005**, *98*, 1172.

16. Jose, J. P.; Thomas, S. In *Physical Chemistry Chemical Physics*; Royal Society of Chemistry, **2014**; Vol. 16, pp 14730.

17. Jose, J. P.; Chazeau, L.; Cavaillé, J. Y.; Varughese, K. T.; Thomas, S. *RSC Adv.* **2014**, *4*, 31643.

18. Zare, Y.; Rhee, K. Y. *Polym. Compos.* **2019**, *40*, 4135.

19. Cavaliere, P.; Jahantigh, F.; Shabani, A.; Sadeghi, B. *Compos. Part B Eng.* **2018**, *146*, 60.

20. Tang, C.; Li, X.; Yin, F.; Hao, J. *IEEE Trans. Dielectr. Electr. Insul.* **2017**, *24*, 2400.

21. Qi, D.; Gao, F.; Chen, Z.; Cui, Z.; Wang, G.; Wang, N.; Zhang, Y.; Qu, G.; Cao, Z. *Colloids Surfaces A Physicochem. Eng. Asp.* **2017**, *523*, 106.

22. Abraham, J.; Thomas, J.; Kalarikkal, N.; George, S. C.; Thomas, S. *J. Phys. Chem. B* **2018**, *122*, 1525.

23. Zare, Y. *Polymer (Guildf).* **2015**, *72*, 93.

24. Jose, J. P.; Thomas, S. *Phys. Chem. Chem. Phys.* **2014**, *16*, 20190.

25. Zare, Y.; Rhee, K. Y. *Appl. Clay Sci.* **2017**, *137*, 176.

26. Zare, Y. *Colloid Polym. Sci.* **2017**, *295*, 363.

27. Zare, Y. *J. Colloid Interface Sci.* **2017**, *486*, 249.

28. Zare, Y.; Rhee, K. Y. *Compos. Sci. Technol.* **2017**, *144*, 18.

29. Pukánszky, B. *Composites* **1990**, *21*, 255.

30. Gigante, V.; Aliotta, L.; Phuong, V. T.; Coltelli, M. B.; Cinelli, P.; Lazzeri, A. *Compos.*

Sci. Technol. **2017**, *152*, 129.

31. Phuong, V. T.; Gigante, V.; Aliotta, L.; Coltelli, M. B.; Cinelli, P.; Lazzeri, A. *Compos. Sci. Technol.* **2017**, *139*, 127.

32. Zare, Y.; Garmabi, H. *J. Appl. Polym. Sci.* **2012**, *124*, 1225.

33. Hári, J.; Horváth, F.; Móczó, J.; Renner, K.; Pukánszky, B. *Express Polym. Lett.* **2017**, *11*, 479.

34. *Crosslinkable Polyethylene*; Thomas, J.; Thomas, S.; Ahmad, Z., Eds.; Materials Horizons: From Nature to Nanomaterials; Springer Singapore: Singapore, **2021**.

35. Thomas, J.; Thomas, M. E.; Thomas, S. **2021**, 1.

36. Effects of Kenaf Loading on Processability and Properties of Linear Low-Density Polyethylene/Poly (Vinyl Alcohol)/Kenaf Composites | Pang | BioResources. https://ojs.cnr.ncsu.edu/index.php/BioRes/article/view/BioRes_10_4_7302_Pang_Kenaf_Loading_Processability_Polyethylene (accessed April 29, 2021).

37. Feifel, S. C.; Lisdat, F. *J. Nanobiotechnology* **2011**, *9*, 59.

38. Zhang, L.; Zhou, Y.; Cui, X.; Sha, Y.; Le, T. H.; Ye, Q.; Tian, J. *IEEE Trans. Dielectr. Electr. Insul.* **2014**, *21*, 1554.

39. Li, X.; Schneider, K.; Kretzschmar, B.; Stamm, M. *Macromolecules* **2008**, *41*, 4371.

40. Wang, K. H.; Chung, I. J.; Jang, M. C.; Keum, J. K.; Song, H. H. *Macromolecules* **2002**, *35*, 5529.

41. Zhu; Zhao; Han; Wang; Wang; Liu; Xie; Zhu *Energies* **2019**, *12*, 2994.

42. Krill, C. E.; Birringer, R. *Philos. Mag. A Phys. Condens. Matter, Struct. Defects Mech. Prop.* **1998**, *77*, 621.

43. Nóbrega, A. M.; Martinez, M. L. B.; De Queiroz, A. A. A. *J. Mater. Eng. Perform.* **2014**, *23*, 723.

44. Mandelkern, L. Crystallization kinetics of homopolymers: Overall crystallization: A review. *Biophys. Chem.* **2004**, *112*, 109–116.

45. Hoffman, J. D.; Miller, R. L. Kinetics of crystallization from the melt and chain folding in polyethylene fractions revisited: Theory and experiment. *Polymer (Guildf).* **1997**, *38*, 3151–3212.

46. Furushima, Y.; Nakada, M.; Murakami, M.; Yamane, T.; Toda, A.; Schick, C. *Macromolecules* **2015**, *48*, 8831.

47. Wunderlich, B. *Thermal analysis of polymeric materials*; Springer Berlin Heidelberg, **2005**.

48. Zare, Y.; Rhee, K. Y. *JOM* **2019**, *71*, 3989.

49. Liu, S. P. *J. Ind. Eng. Chem.* **2014**, *20*, 2401.

50. Kuan, H. C.; Kuan, J. F.; Ma, C. C. M.; Huang, J. M. *J. Appl. Polym. Sci.* **2005**, *96*, 2383.

51. Gulmine, J. V.; Akcelrud, L. *J. Appl. Polym. Sci.* **2004**, *94*, 222.

52. Zare, Y. *Mech. Mater.* **2015**, *85*, 1.

53. Lazzeri, A.; Phuong, V. T. *Compos. Sci. Technol.* **2014**, *93*, 106.

54. Thomas, M. E.; Vidya, R.; Thomas, J.; Ahmad, Z. **2021**; pp 299.

55. Zare, Y. *RSC Adv.* **2016**, *6*, 57969.

56. Zare, Y. *Compos. Part B Eng.* **2015**, *73*, 111.

57. Leidner, J.; Woodhams, R. T. *J. Appl. Polym. Sci.* **1974**, *18*, 1639.

58. Nicolais, L.; Narkis, M. *Polym. Eng. Sci.* **1971**, *11*, 194.

59. Yang, L.; Wang, X.; Qiu, Q.; Gao, J.; Tang, C. *Mater. Chem. Phys.* **2021**, *260*, 124124.

60. Roy, M.; Reed, C. W.; MacCrone, R. K.; Schadler, L. S.; Nelson, J. K.; Keefe, R.; Zenger, W. *Proc. Int. Symp. Electr. Insul. Mater.* **2005**, *1*, 223.

61. Hande, V. R.; Rath, S. K.; Rao, S.; Praveen, S.; Sasane, S.; Patri, M. *J. Memb. Sci.* **2016**, *499*, 1.

62. Meera, A. P.; Said, S.; Grohens, Y.; Thomas, S. *J. Phys. Chem. C* **2009**, *113*, 17997.

63. Joy, J.; George, E.; Thomas, S.; Anas, S. *New J. Chem.* **2020**, *44*, 4494.

64. Jiang, H.; Zhang, X.; Gao, J.; Guo, N. *Energies 2021, Vol. 14, Page 1235* **2021**, *14*, 1235.

65. Nedjar, M. *J. Appl. Polym. Sci.* **2009**, *111*, 1985.

66. Zawar, S.; Atiq, S.; Tabasum, M.; Riaz, S.; Naseem, S. *J. Saudi Chem. Soc.* **2019**, *23*, 417.

67. Wu, C.; Deshmukh, A. A.; Li, Z.; Chen, L.; Alamri, A.; Wang, Y.; Ramprasad, R.; Sotzing, G. A.; Cao, Y. *Adv. Mater.* **2020**, *32*, 2000499.

68. Jlassi, K.; Chandran, S.; Poothanari, M. A.; Benna-Zayani, M.; Thomas, S.; Chehimi, M. M. *Langmuir* **2016**, *32*, 3514.

69. Ma, Z.; Huang, X.; Jiang, P.; Wang, G. *J. Appl. Polym. Sci.* **2010**, *115*, 3168.

70. Zhao, G.; Ishizaka, T.; Kasai, H.; Hasegawa, M.; Furukawa, T.; Nakanishi, H.; Oikawa, H. *Chem. Mater.* **2009**, *21*, 419.

71. Leu, C. M.; Chang, Y. Te; Wei, K. H. *Macromolecules* **2003**, *36*, 9122.

72. Thomas, J.; Francis, B.; Thomas, S.; Schechter, A.; Grynszpan, F. *Solid State Ionics* **2021**, *370*, 115731.

73. Grabowski, C. A.; Fillery, S. P.; Westing, N. M.; Chi, C.; Meth, J. S.; Durstock, M. F.; Vaia, R. A. *ACS Appl. Mater. Interfaces* **2013**, *5*, 5486.

74. Tanaka, T.; Kozako, M.; Fuse, N.; Ohki, Y. *IEEE Trans. Dielectr. Electr. Insul.* **2005**, *12*, 669.

75. Roy, M.; Nelson, J. K.; MacCrone, R. K.; Schadler, L. S.; Reed, C. W.; Keefe, R.; Zenger, W. *IEEE Trans. Dielectr. Electr. Insul.* **2005**, *12*, 629.